THE JOURNAL OF PHYSICAL CHEMISTRY C
A JOURNAL OF THE AMERICAN CHEMICAL SOCIETY

pubs.acs.org/JPCC

Article

Aliovalent-Doping Effects on the Surface Activity of Mesoporous CeO_2 toward Nerve Agent Simulant DMMP Decomposition

Tianyu Li, Lucas Algrim, Monica McEntee, Roman Tsyshevsky, Matthew Leonard, Erin M. Durke, Christopher Karwacki, Maija M. Kuklja, Michael R. Zachariah, and Efrain E. Rodriguez*

Cite This: *J. Phys. Chem. C* 2022, 126, 17923–17934

Read Online

ACCESS | Metrics & More | Article Recommendations | Supporting Information

ABSTRACT: Aliovalent doping is frequently used as a strategy to modify the chemical and physical behavior of fluorite-type CeO_2. Ceria has been proven to be active toward room-temperature decomposition of dimethyl methylphosphonate (DMMP), a chemical warfare agent simulant. Here, we systematically explore how alio-doping influences the interaction between mesoporous CeO_2 and DMMP molecules at room temperature and under ambient conditions. We dope mesoporous CeO_2 with 10, 20, and 30% Y^{3+} and perform in situ diffuse reflectance infrared Fourier transform spectroscopy and ex situ solid-state ^{31}P NMR to understand surface speciation after exposing the mesoporous metal oxides to DMMP. We also monitor the reaction product methanol via mass spectrometry. All the measurements consistently show that doping with Y^{3+} gradually impedes the reactivity of mesoporous CeO_2 toward DMMP decomposition. X-ray photoelectron spectroscopy and CO adsorption infrared indicate that Y^{3+} doping may cause decreased activity of mesoporous CeO_2 by increasing hydroxylation and limiting the exposure of the active (111) surface. La^{3+}- and Gd^{3+}-doped mesoporous CeO_2 also display similar decreased activity toward DMMP decomposition compared with pure mesoporous CeO_2, implying a general trend of impact of alio-doping on CeO_2 interacting with DMMP. We conclude that control of surface hydroxylation and preferred crystal surface exposure are key toward improving the performance of CeO_2 toward DMMP dissociation.

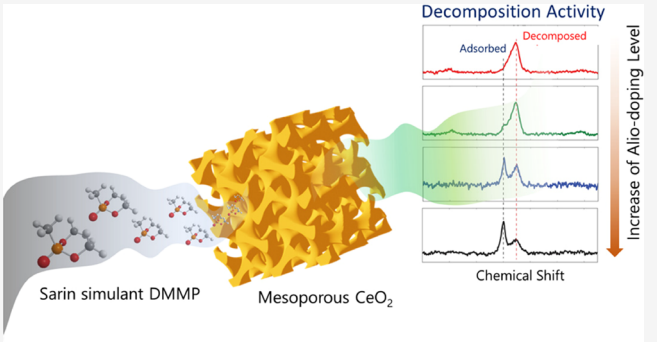

1. INTRODUCTION

Developing materials for combating chemical warfare agents (CWAs), especially nerve agents, is urgently needed due to the concern of the spread of their use in chemical attacks around the world. Based on the specific situation, different types of materials need to be developed to protect civilians against CWAs. To prevent the expansion of usage of CWAs, materials to destroy chemical weapons are needed. Where CWAs have already caused damage, materials to purify the soil and air will be necessary. In active war zones or high-risk areas, highly efficient filter materials in the gas mask or protective coat are required for the protection of military and innocent civilians. An effective filter material to combat nerve agents should strongly adsorb and quickly destroy the nerve agent.

Metal oxides represent potential filter material candidates for protection against CWAs. Experimentally, since dimethyl methylphosphonate (DMMP) bears resemblance to GB (Sarin, one of CWAs) in structure (displayed in Scheme 1) and vapor pressure, it is commonly used as a simulant of GB to estimate the adsorption and decomposition performance of GB on various adsorbent materials. Therefore, studying the interactions of metal oxides with DMMP remains topical.[1−15] The surface polarity and diverse surface chemistry toward different molecules of metal oxides can lead to a great performance toward DMMP adsorption and decomposition. In addition, fabrication of the mesoporous metal oxides can overcome the low-surface-area nature of conventional metal oxide materials as adsorbents.

Scheme 1. Structure of (a) Sarin (GB) and Its Simulant (b) Dimethyl Methylphosphonate (DMMP)

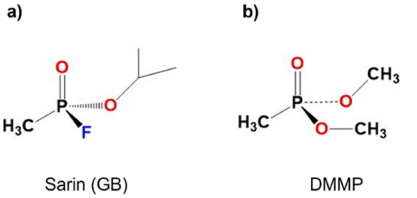

Received: July 9, 2022
Revised: September 30, 2022
Published: October 14, 2022

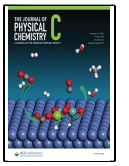

Another advantage that metal oxides bear is their promising tunability. Doping is a commonly used strategy to adjust the physical and chemical properties of various metal oxides. While extensive categories of phase-pure metal oxides have been studied for their interactions with DMMP,[1−15] little effort has been made on tuning the metal oxides to systematically alter their activities toward DMMP.

Fluorite-type CeO_2 draws extensive attention due to its great performance in extensive catalytic reactions and ionic conductivity.[16−20] Previous studies using single crystal surfaces of CeO_2 and our own on mesoporous CeO_2 demonstrate their effective activity toward DMMP decomposition and other phosphorus containing compounds at room temperature.[21−28] CeO_2 is among the most tunable metal oxides due to its structural tolerance. Not only can neighboring rare earth metal elements (e.g., Gd and La) be doped into CeO_2,[29,30] but so can alkaline-earth[31] and transition metal elements.[32,33] Doping has been proved to be an extremely effective way to adjust various properties of CeO_2 since it can modulate its band gap by adjusting its lattice parameters, introducing impurity (donor or acceptor) bands, or altering the photocatalytic/electrocatalytic activities.[18,19,30,34−36] Lattice distortion or oxygen vacancies can also be introduced into CeO_2 through doping, leading to a change of ionic conductivity.[20,37,38]

What interests us most in this study is how doping strongly influences the surface properties of CeO_2. Dopants can also stabilize various surfaces of CeO_2,[39,40] which might preferentially expose different crystallographic surfaces in the synthesis of ceria. Doping can change the absorption strength of water too and thus affect the hydrophilic behavior of CeO_2.[41−44] The dissociation energy barrier of some molecules such as H_2O and CO on the CeO_2 surfaces can be greatly modulated via doping.[45−50] Ceria's tolerance for various dopants and the consequent strong influence of doping on the properties of CeO_2 imply that it can be an effective strategy to achieve greater surface activities of CeO_2 for DMMP adsorption and decomposition. Extensive research needs to be conducted to find the best doping strategy for the application of DMMP adsorption and decomposition.

Here, we aimed at understanding how a general alio-doping (low valence doping) influences the interaction between CeO_2 and DMMP. Thus, we synthesized mesoporous CeO_2 doped with various amounts (10, 20, and 30%) of Y^{3+}, Gd^{3+}, and La^{3+}. Each of these metals neighbor Ce in the periodic table and thus displays a similar ionic radius and chemical activity to Ce^{4+}. We focus most of our study on the Y^{3+}-doped series. We systematically present the interaction between Y^{3+}-doped CeO_2 materials and DMMP with mass spectroscopy, diffuse reflectance infrared Fourier transform spectroscopy (DRIFTS), and ^{31}P solid-state nuclear magnetic resonance (NMR). All measurements consistently indicate that Y^{3+} doping decreases the activity of DMMP decomposition compared with pure mesoporous CeO_2. We also observe a similar trend for Gd^{3+}- and La^{3+}-doped mesoporous CeO_2. The consistency across all three series implies a universal correlation between alio-doping of CeO_2 and DMMP decomposition activity under ambient conditions. We discuss the implications of such a correlation on the design of future mesoporous materials for the adsorption and defeat of dangerous toxins such as CWAs.

2. METHODS

2.1. Synthesis of Templated Mesoporous CeO_2. Mesoporous CeO_2 was synthesized via a nanocasting method which was previously reported.[51,52] The silica template KIT-6 was first prepared via a reported method,[53] on which 85 °C was used as the aging temperature during the KIT-6 synthesis. In our typical synthesis of mesoporous CeO_2, 0.5000 g of as-prepared KIT-6 silica was initially dispersed in 20.0 mL of 95% ethanol. Then, 1.302 g of $Ce(NO_3)_3{\cdot}6H_2O$ (0.003 mol) was also dissolved in the same solution. We stirred the mixture at room temperature until all the solvents inside evaporated and the mixture became a dry powder. The powder was later transferred to a glass vial (diameter ∼ 5 mm) and under calcination at 560 °C for 6 h (ramping rate 1 °C/min) to form a CeO_2/KIT-6 composite. The CeO_2/KIT-6 composite was soaked in a 2 M NaOH solution 3 times at 80 °C overnight to fully remove the silica template. After being washed with distilled water 3 times and with ethanol 2 times, the final mesoporous CeO_2 product was dried in air at 80 °C overnight and 150 °C for another day. For the synthesis of Y^{3+}-, La^{3+}-, Gd^{3+}-substituted samples, all the procedures are the same as the synthesis of pure mesoporous CeO_2, except that the 10, 20, and 30% mol ratios of cerium nitrate salt were replaced by the same moles of a Y, La, or Gd nitrate salt.

2.2. Materials Characterization. Transmission electron microscopy (TEM) images were taken using JEOL JEM 2100 LaB6 TEM equipment, and X-ray small-angle scattering (SAXS) patterns were collected with a Xenocs Xeuss SAXS/WAXS/GISAXS small-angle system. The nitrogen adsorption isotherms were measured using a Micromeritics ASAP 2020 Porosimeter Test Station. The surface area was calculated by applying the Brunauer−Emmett−Teller equation on adsorption data obtained at P/P_0 between 0.05 and 0.35. The pore size distributions were then calculated by analyzing the adsorption branch of the N_2 sorption isotherm using the Barret−Joyner−Halenda method. Powder XRD patterns were recorded on a Bruker D8 Advance diffractometer, with Cu Kα/Kβ radiation. The mesoporous CeO_2 samples with 10, 20, and 30% Y^{3+} doping were also examined by time-of-flight neutron diffraction. The neutron diffraction patterns were collected at 300 K using a nanoscale-ordered materials diffractometer at the Spallation Neutron Source, Oak Ridge National Laboratory. Rietveld refinement was performed on the diffraction patterns using TOPAS 5.[54] Ce 3d and O 1s X-ray photoelectron spectroscopy (XPS) spectra were collected with a Kratos Axis 165 X-ray photoelectron spectrometer operating in hybrid mode using Al Kα monochromatic X-rays at 280 W. For the Y^{3+}-, Gd^{3+}-, La^{3+}-doped CeO_2 samples, Y 3d, Gd 3d, and La 3d spectra were also collected on the corresponding samples. All XPS spectra were calibrated to the C 1s peak at 284.80 eV. All spectral fittings were performed using CasaXPS. The Shirley background was used for background subtraction. The peak shape profile of 30% Gaussian +70% Lorentzian was applied for the fitting.

2.3. CO Adsorption TIR. Carbon monoxide (CO) adsorption studies on doped CeO_2 were performed in a high vacuum chamber with a base pressure at 3×10^{-9} Torr. A more detailed description of the vacuum chamber is provided elsewhere.[55] Each sample was pressed into a 0.004″ thick W-grid and attached to the sample mount via stainless-steel clamps connected to copper rods. The copper rods were attached to a power supply allowing for resistive heating of the sample up to ∼1000 K at a resolution of ±0.1 K. Before introducing CO into the vacuum chamber, the sample was heated up to 450 K for 30 min in order to remove any H_2O and hydrocarbon impurities. After heating, the surface was

https://doi.org/10.1021/acs.jpcc.2c04853
J. Phys. Chem. C 2022, 126, 17923−17934

cooled down with LN_2 (~140 K) and an IR spectrum was taken of the CeO_2 sample. An IR spectrum was taken of the W-grid without any CeO_2 powder and used as the background. Each IR spectrum contains an average of 256 interferograms at a resolution of 2 cm^{-1}. Subsequently, 10^{-2} Torr of CO vapor was introduced into the vacuum chamber. An IR spectrum was taken and was subtracted from the IR spectrum of CeO_2 prior to CO exposure. The subtracted spectrum represents a difference spectrum showing the CO adsorption on the CeO_2 surface.

2.4. In Situ DRIFTS Measurement of DMMP Adsorption/Decomposition on Doped Mesoporous CeO_2 at Room Temperature. A Harrick Scientific Praying Mantis DRA optical accessory was used with an associated Harrick Scientific high-temperature reaction chamber HVC-DRP-5 and temperature controller unit (110 V, ATC-024-3) for the DRIFTS measurements. Before the DMMP exposure experiment, mesoporous CeO_2 powder was heated under the 25 mL/min Ar flow at 200 °C for 2 h to remove as much physisorbed water as possible and then cooled to room temperature. We were mainly interested in the interaction between mesoporous CeO_2 and strongly adsorbed DMMP molecules. In addition, we wanted to minimize the DMMP contamination on our DRIFTS system. Thus, we applied a swift injection approach to introduce DMMP into the DRIFTS cell containing mesoporous CeO_2 powder. In our typical experiment, mesoporous CeO_2 powder in the cell was under constant 25 mL/min Ar flow all the time, and 2 mL of saturated DMMP vapor carried by N_2 was quickly injected into the system using a delay controlled electronic injector. An illustration of such a system is provided in the Supplementary Information. The injections occurred every 20 min. During the 20 min gap, DRIFTS spectral scans were collected every 30s, allowing the strong interaction between the substrate (CeO_2) and molecules (DMMP) to be observed. A total of 10 DMMP injections were performed.

2.5. Ex Situ Solid-State 31P NMR Measurement of DMMP Adsorption/Decomposition on Doped Mesoporous CeO_2 at Room Temperature. For the ex situ measurement, 50 mg of each powder sample (dried in Ar flow at 150 °C for 2 h) was exposed under saturated DMMP vapor for 30 min at room temperature, followed by evacuation under vacuum for 10 min to remove the nonadsorbed or loosely adsorbed DMMP in the material. Right after the ex situ DMMP experiment, solid-state natural abundance ^{31}P NMR spectra of magic angle spinning (MAS) samples were acquired with a Bruker AVANCE NEO 500 MHz NMR spectrometer using the combination of standard cross-polarization with proton spinal-64 decoupling. Samples were packed in 3.2 mm o.d. rotors and run in a Bruker double resonance MAS probe. Proton 90° pulse widths of 2.5 μs, contact times of 3.5 ms, and pulse delays of 4 s with 1025 scans were used to acquire ^{31}P NMR spectra. Phosphorus-31 chemical shifts were referenced with respect to 85% H_3PO_4 (0 ppm) by setting $\delta(^{31}P)$ of ammonium dihydrogen phosphate at 0.81 ppm. Spectra of MAS samples were acquired at ambient temperature with a spinning frequency of 8 kHz, and spinning sidebands were confirmed by running experiments with a different spinning rate.

2.6. Detection of DMMP Decomposition on Doped Mesoporous CeO_2 via Mass Spectrometry. Mass spectrometry was used to detect reaction products (majorly methanol) from the interaction of doped mesoporous CeO_2 and DMMP. The measurements made with a mass spectrometer used an experimental setup described in the previous work[56] but again briefly described here. Before analysis with a mass spectrometer, the CeO_2 sample was heated to 200 °C to remove any potential surface contaminants. Three mass flow controllers regulate the flow of dry argon, argon saturated with water, and DMMP, all of which are combined to produce a 35 mL/ min total flow that is 0.4 P/P_0 DMMP and 4% relative humidity at room temperature. The combined flow is passed into a 4.7625 mm (3/16″) ID quartz tube which holds the CeO_2 sample, supported by inert glass wool. The quartz tube is heated at 10 °C/min to 325 °C and held for 3 h before cooling to room temperature, where it dwells for approximately 7 h before heating again. This temperature cycle was repeated multiple times. Downstream from the material, a capillary line sampled the gas mixture into a quadrupole mass spectrometer, and the methanol signal (m/z 31) was monitored. All-time traces were normalized to m/z 36 (an isotope of argon) to minimize the effects of signal drift.

3. RESULTS AND DISCUSSION

3.1. Characterization. To exclude the possible influence of pore structure and surface area on the interaction between DMMP and CeO_2 samples, we used the same batch of the KIT-6 silica template for all the syntheses of doped and pure mesoporous CeO_2, ensuring that all the samples to be tested possess very similar morphologies in the nanoscale. Such similarity was confirmed through TEM, SAXS, and nitrogen adsorption measurement. As shown in TEM (Figures S1–S3), all the mesoporous samples display very similar ordered porous structures. Clear diffraction peaks are visible in the SAXS measurement (Figure 1b for Y^{3+} doped, Figures S4 and S5 for Gd^{3+} and La^{3+} doped), confirming that ordered pore structures were preserved for pure and doped mesoporous CeO_2. No major diffraction pattern changes or peak shift is observed through SAXS, indicating that doping with Y^{3+}, La^{3+}, and Gd^{3+} does not have a strong impact on the pore structure formation.

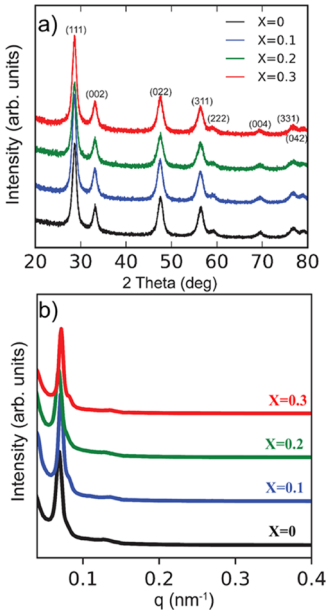

Figure 1. (a) XRD and (b) SAXS characterizations: mesoporous $Ce_{1-x}Y_xO_{2-\delta}$ (x = 0, 0.1, 0.2, 0.3).

https://doi.org/10.1021/acs.jpcc.2c04853
J. Phys. Chem. C 2022, 126, 17923−17934

Nitrogen adsorption isotherms and the corresponding pore size distribution curve (inset) for all samples are shown in Figures S6–S8. The extracted surface area and mean pore size of CeO_2 samples are listed in Table S1. Doped as well as pure mesoporous CeO_2 displayed relatively high and similar surface area (around 130 ± 20 m^2/g), and the mean pore size deviates very little between each sample (~3 nm).

Figures 1a and S9 present the XRD patterns of as-synthesized mesoporous samples. We observe a pure phase of cubic fluorite-type structure ($Fm\bar{3}m$) for all the samples. The broadened diffraction peak indicates low crystallinity and nanocrystalline grains. The refined Lorentz grain sizes are very similar for each sample, ranging from 8 to 12 nm. Theoretically, the lattice parameter will alter upon substituting/doping cations in the CeO_2 system due to the ionic size difference between Ce^{4+} and other cations.[30,57] Studies have shown that 10% doping of Y^{3+}, La^{3+}, or Gd^{3+} is enough to see a lattice parameter deviation from pure CeO_2 in the samples with very high crystallinity.[57] In our mesoporous systems, the extremely broadened Bragg peaks, due to low crystallinity as well as possible strain, mask any difference between the doped and pure CeO_2 samples. The refined lattice parameter for each sample is nearly the same within error.

We selected the 10, 20, and 30% Y^{3+}-doped samples to examine with neutron diffraction since neutrons are more sensitive to oxygen atoms with respect to the heavy metal atoms compared to X-ray diffraction. The neutron diffraction patterns are shown in Figure S10. No impurity phase was observed for neutron patterns. Even for neutron diffraction, low crystallinity also causes a severe peak broadening, posing difficulty in data analysis. Our Rietveld refinement results on neutron diffraction show a decreasing trend of lattice parameters upon the increasing amount of Y^{3+} doping, which resembles what was reported in a previous study.[58] During the refinement, we deliberately fixed the oxygen occupancy at 100% and watched the change of atomic displacement parameters (ADPs) of Ce and O atoms for each sample. As Y^{3+} doping increases, the ADPs of Ce and O both increase (Figure S10), indicating an increase of static disorder in the sample due to an increase of oxygen vacancies.[58] Thus, as expected, alio-doping Y^{3+} into our mesoporous CeO_2 system increases the concentration of oxygen vacancies in the bulk. As more Y^{3+} doped into the CeO_2 lattice, our neutron diffraction measurement can detect the increase of oxygen vacancies in the bulk. Gd^{3+} and La^{3+} are very similar to Y^{3+} in terms of valence and chemical reactivity. Based on our neutron measurements on Y^{3+}-doped CeO_2 and the reports on doped CeO_2 with high crystallinity,[57,59] we infer that increasing Gd^{3+} and La^{3+} doping also increases the concentration of oxygen vacancies in the bulk for mesoporous CeO_2, just as Y^{3+} does in mesoporous CeO_2.

We also performed XPS measurements to understand the elemental valence states and ratio on the surface. Ce 3d XPS is displayed in Figures S11 and S12. Strictly following the reported fitting parameters,[60] we fit the Ce 3d spectra with just Ce^{4+} components for pure and all doped mesoporous CeO_2 samples, implying that doping of Y^{3+}, La^{3+}, or Gd^{3+} does not influence the valence state of CeO_2 in our mesoporous system. Therefore, Ce^{4+} instead of Ce^{3+} dominates the surface states for all the samples.

The O 1s XPS spectrum (Figures S13 and S14) shows two major types of oxygen, namely, lattice oxygen (O^{2-}) at 529.3 eV and surface oxygen (−OH) at 531.5 eV, common for metal oxides. The statistics of the ratio between surface oxygen (−OH) and total oxygen fitted from XPS O 1s spectra are displayed in Figure 1a. We observed an increasing trend of hydroxylating level (ratio of OH) on the surface as the doping level rises for the mesoporous CeO_2 samples. Such a trend exists for all Y^{3+}-, La^{3+}-, Gd^{3+}-doped systems. It is also clear that a low level of doping (10%) shows little difference with pure CeO_2 in terms of OH ratios on the surface.

We attribute the increase of the hydroxylating level upon doping to the stabilization of oxygen vacancies on the surface. We expected bulk oxygen vacancy levels to rise upon increasing alio-doping and for the same effect to take place on the surface. However, under the ambient synthetic conditions, surface oxygen vacancies are not stable and will be stabilized by uptake of molecules such as CO_2 and H_2O.[41−44,46,47,49] In our case, the defective surface is stabilized by environmental H_2O, resulting in the formation of OH. In a low doping level case, the destabilization energy of oxygen vacancies is not high enough to allow the formation of OH groups. Thus, 10% doping does not alter the hydroxylating level in our mesoporous CeO_2 system.

From Figure 2a, we also find that the dopants have different levels of impact on surface hydroxylation, with Y^{3+} having the strongest influence and Gd^{3+} the weakest. Such variation of the impact of dopants on surface hydroxylation results from different destabilization energies of dopants on the crystal lattices.[41] The XPS 3d spectra of dopants (Y^{3+}, La^{3+}, and Gd^{3+}) were also recorded (Figure S15), and we looked at the dopant/Ce^{4+} ratio change with the increase of the doping level (Figure 2b). As is expected, the dopant ratio (Y^{3+}, La^{3+}, and Gd^{3+}) on the surface rises when the doping level increases in bulk. However, for each of the doping levels, the dopant ratio on the

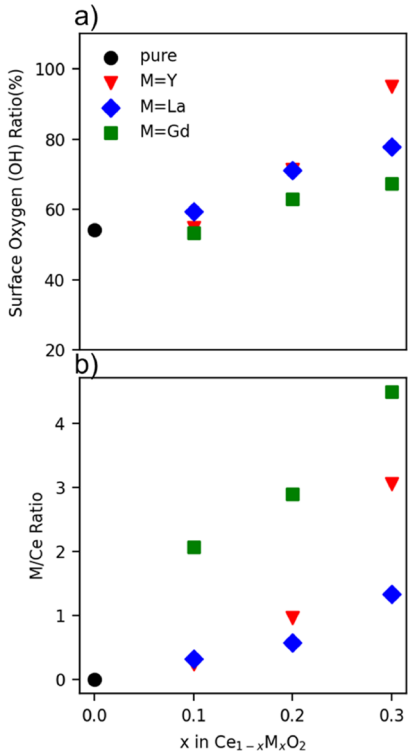

Figure 2. (a) Surface oxygen/lattice oxygen ratio. (b) Dopant/Ce ratio of mesoporous $Ce_{1-x}M_xO_{2-\delta}$ (x = 0, 0.1, 0.2, 0.3) extracted from XPS measurement.

https://doi.org/10.1021/acs.jpcc.2c04853
J. Phys. Chem. C 2022, 126, 17923−17934

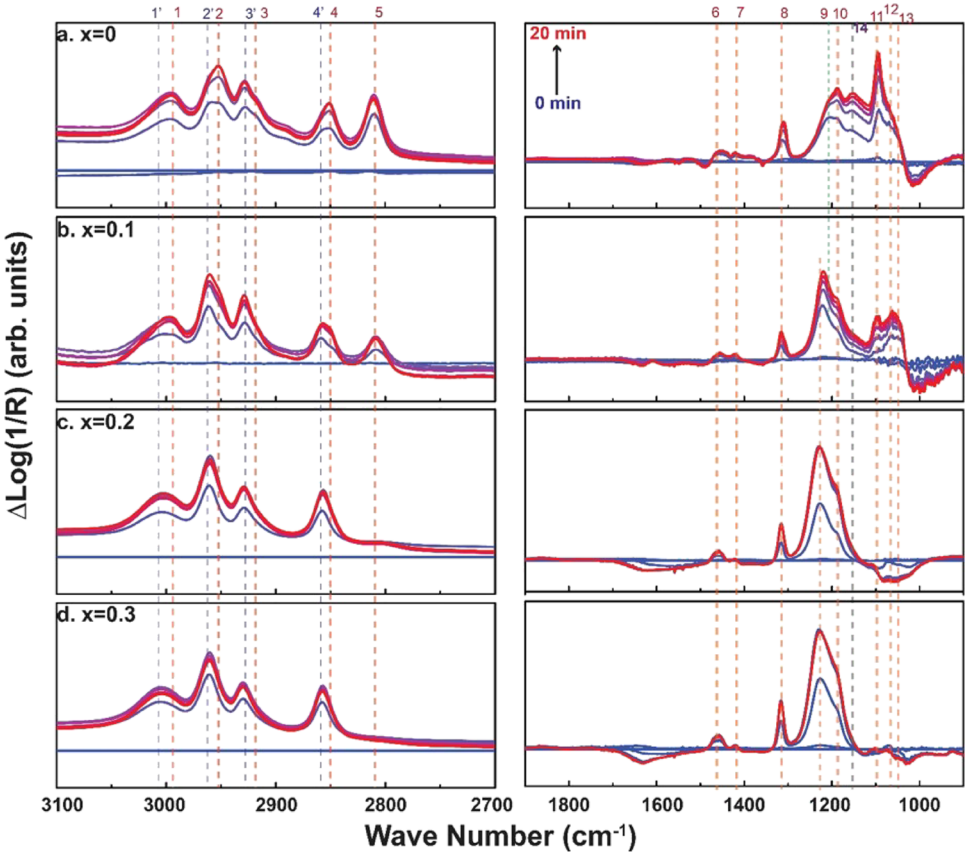

Figure 3. (a–d) In situ DRIFTS measurement of $Ce_{1-x}Y_xO_{2-\delta}$ (x = 0, 0.1, 0.2, 0.3) upon DMMP injections.

Table 1. Assignment of IR Peaks upon DMMP Dosing onto Mesoporous $Ce_{1-x}Y_xO_{2-\delta}$ (x = 0, 0.1, 0.2, 0.3) from DRIFTS Characterization. Green color indicates the bands from the decomposition of DMMP. Red color indicates the band that shows a significant shift between undoped and doped CeO_2. Blue color indicates the subbands of the major modes.

vibration mode	position	x=0	x=0.1	x=0.2	x=0.3
ν_a (PCH_3)	1	2996	2996	x	x
	1'	3003	3004	3003	3004
ν_a (OCH_3)	2	2952	2952	x	x
	2'	2960	2959	2960	2960
ν_s (PCH_3)	3	2905	2905	x	x
	3'	2928	2928	2929	2929
ν_s (PCH_3)	4	2851	2851	x	x
	4'	2856	2856	2857	2857
ν_s ($MOCH_3$)	5	2811	2808	x	x
δ_a (OCH_3) and δ_s (OCH_3)	6	1467	1467	1467	1467
δ_a (PCH_3)	7	1421	1421	1421	1421
δ_s (PCH_3)	8	1314	1314	1314	1314
ν (P=O)	9	1204	1220	1228	1228
ρ(OCH_3)	10	1188	1190-1192	1190	1190
ν (OPO)	11	1096	1100	x	x
ν_a (C-O)	12	1070	1069	x	x
ν_s (C-O)	13	1047	1047	x	x
	14	1116-1170	1116-1170	x	x

surface exceeds the dopant ratio that we added in CeO_2 during the synthesis (bulk). The dopant ratio on the surface is more than twice that in the bulk. Since we observed no impurity phases in our diffraction measurement, we exclude the phase

https://doi.org/10.1021/acs.jpcc.2c04853
J. Phys. Chem. C 2022, 126, 17923−17934

separation of bulk as the cause. In the alio-doping metal oxides, enrichment of dopants is not rare and has been reported on some metal oxide systems.[61−67] The dopant enrichment on the surface is usually driven by lowering the surface energy (i.e., stabilization).[66]

3.2. Influence of Y Doping on the Activity of Mesoporous CeO_2 toward DMMP Decomposition at Room Temperature. We focus on the Y^{3+}-doped mesoporous CeO_2 samples to understand how alio-doping influences their interaction with DMMP at room temperature. We first performed DRIFTS study and made direct comparisons within mesoporous CeO_2 doped with different amounts of Y^{3+}. Figure 3 shows the in situ DRIFTS spectra of pure and Y^{3+}-doped mesoporous CeO_2, which was taken immediately following the first injection of DMMP. Assignment of the IR bands is presented in Table 1. Bands at locations 1−4, 6−10, and 12−13 belong to the vibration modes of intact DMMP.[2,4,28] Band 5 (~2810 cm^{-1}) corresponds to C−H stretching modes of the OCH_3 group when it directly bonds to a metal center.[4,5,68] Band 11 (~1096 cm^{-1}) and part of the broad band 14 (1116−1170 cm^{-1}) represent stretching modes of the O−P−O species.[5,9,68] The appearance of bands 5, 11, and 14 (formation of M−OCH_3 and O−P−O species) indicates dissociation of DMMP on the surface. The dissociation is believed to go through a P−OCH_3 bond breaking process.[4,28,68] Interestingly, as shown in Figure 3, we observed that the relative intensities of bands 5, 11, and 14 (M−OCH_3 and O−P−O species) undergo a significant decrease as the doping level increases compared with other bands. Such a decrease of intensity indicates the diminishing decomposition activity of DMMP on the surface as the doping level increases.

Band 9 around 1204 cm^{-1} correlates with the P═O stretching mode of adsorbed and intact DMMP. For all the doped series, we found this band to undergo a blue shift (to a high wavenumber) as the doping level rises (Figure 3 and Table 1). It is commonly believed that DMMP adsorbs on the surface through its P═O bond.[8,9,11,12,69,70] The P═O group can then contribute some of its electron density upon adsorption, leading to a less polar or weaker P═O bond.[71,72] Conversely, a blue shift of P═O stretching modes means a more polar P═O bond, implying weaker DMMP adsorption. Thus, we conclude that the alio-dopant not only leads to a decreased activity of DMMP decomposition but also weakens DMMP adsorption on the surface of mesoporous CeO_2.

Bands 1−4 are the C−H stretching modes of the −CH_3 part of the DMMP molecule. Through the comparison with doped samples, we found that these bands are all accompanied by a "sideband" in the lower wavenumber region (indicated as 1′, 2′, 3′, and 4′, redshift) as shown in Figure 3 and Table 1. Interestingly, those sidebands gradually fade as the concentration of dopants increases, like what has happened on bands 5, 12, and 14. We did not find any mention of a similar observation in other DMMP adsorption studies. We speculate that those side bands may come from the C−H stretching modes of the decomposition product of DMMP (such as MMP). Another possibility would be the C−H stretching modes of a more strongly adsorbed DMMP molecule. As in the P═O bond, stronger interaction (adsorption) of DMMP on the surface might also activate the C−H bonds (weaker bonding), leading to a redshift of the IR bands.[71,72]

Solid-state NMR provides an alternative way to observe the decomposition activity of DMMP. We examined the ^{31}P NMR spectra of the mesoporous CeO_2 series after their interaction with gas-phase DMMP for 30 min. The phosphorus atom will have different chemical environments between the intact DMMP molecule and dissociated species. Thus, a different chemical shift can be observed in ^{31}P NMR. The ^{31}P NMR spectra of Y^{3+}-doped series are shown in Figure 4. We were

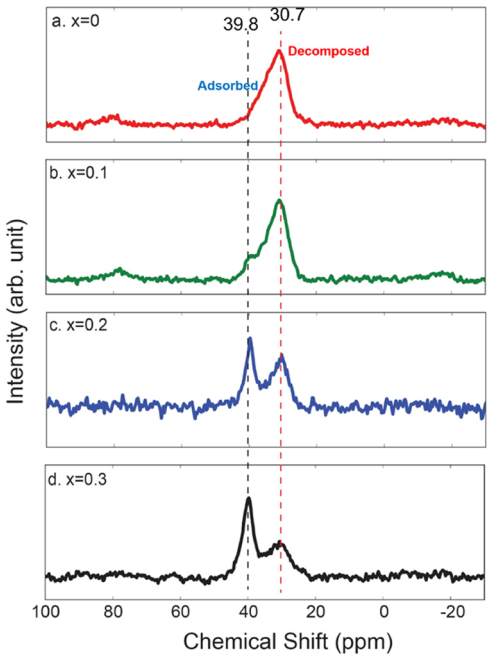

Figure 4. (a−d) Ex situ 31P solid-state NMR measurement of mesoporous $Ce_{1-x}Y_xO_{2-\delta}$ (x = 0, 0.1, 0.2, 0.3) after DMMP dosing.

able to identify three major peaks based on the previous solid-state NMR study on DMMP interacting solids.[73−76] The peak located at 39.8 ppm corresponds to DMMP adsorbed through the hydrogen bond and the one at 34 ppm from adsorbed DMMP. The peak around 30.7 pm is adsorbed MMP or MPA, which is the dissociation product of DMMP after -OCH_3 is cleaved from it.[73−76] The relative intensity between 39.8 and 30.7 ppm increases as the doping level increases, implying that less DMMP dissociates on the alio-doped mesoporous CeO_2, confirming what we have observed in the DRIFTS measurement.

Importantly, the DRIFTS and ^{31}P solid-state NMR spectra only allow us to account for the surface species upon DMMP interacting with CeO_2 materials and not the decomposition products leaving the surface. It is possible that such products leave the CeO_2 surface, leading to the decrease of signal of dissociation species in the DRIFTS and NMR measurement. To further confirm that Y^{3+} doping leads to the decreased activity of CeO_2, we used mass spectrometry to detect reaction products. As is discussed earlier and reported previously, DMMP dissociation on CeO_2 surfaces (or other metal oxides) is through a P−OCH_3 bond breaking, leaving O−P−O species and −OCH_3, or methanol if the surface is hydroxylated.[5,10,13,14,28,69,77] The O−P−O species strongly and irreversibly adsorbs on the surface, while −OCH_3 (or methanol) easily desorbs upon heating. Thus, the methanol signal was monitored upon heating cycles under the DMMP vapor flow. Here, we heat the sample to drive out the

https://doi.org/10.1021/acs.jpcc.2c04853
J. Phys. Chem. C 2022, 126, 17923−17934

decomposition product, methanol, for mass spectrometry detection. We realize that the lattice oxygen of CeO_2 will become active and might be involved in the oxidation of DMMP at these elevated temperatures. Oxidative DMMP decomposition at higher temperatures involving lattice oxygen proceeds through a different mechanism from that at room temperature. We observed the formation of CO_2 when the temperature is above 300 °C. However, as mentioned previously, we only focus on the room-temperature activity in this study. In addition, at the measured temperature range, methanol, rather than CO_2, dominates as the detected decomposition species. Thus, we only focus on the methanol signal as the indication of room-temperature decomposition of DMMP. Figure 5 displays the production of methanol

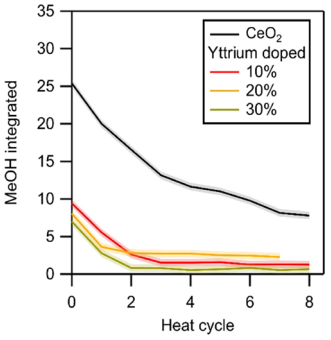

Figure 5. Mass spectrometry measurement of methanol production during heating cycles upon flowing DMMP through mesoporous $Ce_{1-x}Y_xO_{2-\delta}$ (x = 0, 0.1, 0.2, 0.3).

(normalized by surface area) of mesoporous CeO_2 materials integrated at each heating cycle. For pure and all the doped CeO_2, a gradual decrease in methanol production was noted upon each heating cycle, indicating that DMMP decomposition on the CeO_2 surface is a decomposition reaction instead of a hetero-catalytic reaction. The alio-doping does not alter such a behavior either, and the interaction between DMMP and metal oxides is mostly noncatalytic.[7]

Through all the heating cycles, we observed that methanol production from pure mesoporous CeO_2 far exceeds that of the doped samples. As the doping level increases, the production of methanol gradually decreases in very first cycles. In the later cycles, methanol production from doped CeO_2 is very close between different samples, their differences being within the range of error. Again, the decrease of methanol production on doped CeO_2 compared with pure CeO_2 further supports that the surface activity of mesoporous CeO_2 for DMMP degradation is impeded through Y^{3+} doping.

3.3. Origin of the Decreased Activity of Mesoporous CeO_2 upon Y^{3+} Doping. All three different spectroscopic measurements (DRIFTS, solid-state NMR, and mass spectrometry) consistently demonstrate that doping with Y^{3+} gradually decreases the surface activity of mesoporous CeO_2 for DMMP degradation. We can exclude that such a decrease is caused by a change of crystal structure, porosity, or pore structure, since the XRD, nitrogen adsorption, and SAXS characterizations do not significantly vary among the pure and doped mesoporous CeO_2 samples. As a previous IR study indicates, Y_2O_3 nanoparticles are reactive toward DMMP dissociation at room temperature;[5] therefore, it is not likely that the doped Y site on mesoporous CeO_2 behaves as an inactive site. We conclude that a substantial change in the surface properties of mesoporous CeO_2 upon doping occurs, deactivating DMMP dissociation.

3.3.1. Hydroxylation Level and Active Sites. We hypothesize that the primary factor leading to decreased activity upon doping is increased surface hydroxylation. Our previous computational modeling of DMMP interacting with CeO_2 implies that DMMP decomposition on the hydroxylated surfaces of CeO_2 (both (110) and (111)) requires a higher activation energy barrier than on the pristine surfaces,[25] which we summarize in Figure 6. The under-coordinated Ce atoms

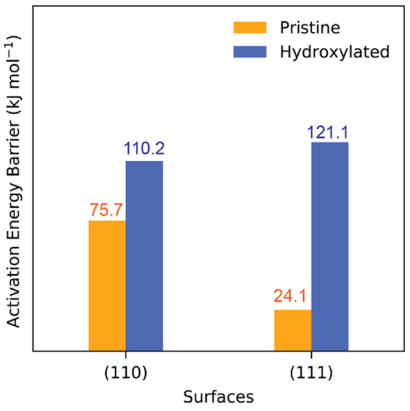

Figure 6. Summarized activation energy barrier for DMMP dissociation on pristine and hydroxylated (110) and (111) surfaces of CeO_2. The results are based on DFT calculation reported previously.[25]

on the pristine surfaces provide sites for a stronger interaction with DMMP molecules either through P═O or P−OCH_3. While on the hydroxylated surfaces, the OH group will bind to under-coordinated Ce atoms, leading to a much less exposure of those active under-coordinated Ce atoms.

As mentioned previously, the XPS results (Figure 2) clearly show the increased weight percent of surface oxygen (OH) upon Y^{3+} doping with the exception that the 10% doped sample remains nearly unchanged. The different hydroxylation levels present in the 20 and 30% doped mesoporous CeO_2 should therefore show decreased activity toward DMMP dissociation, which agrees with our experimental observations.

Our previously study[25] shows that using CO as the probe molecule to characterize the surfaces of CeO_2 with IR is an outstanding to approach to gain more insight on the surfaces of mesoporous CeO_2. Thus, here we used the same method to characterize the surfaces of Y^{3+}-doped mesoporous CeO_2. Pure mesoporous CeO_2 and all Y^{3+}-doped CeO_2 are dosed with CO, and then, IR spectroscopy was applied to detect CO stretching modes. The CO adsorption IR results are shown in Figure 7a. Two major characteristic peaks are observed for pure and Y^{3+}-doped mesoporous CeO_2, which represent CO stretching modes when CO is adsorbed on the (110) and (111) surfaces.[78,79] These two stretching peaks imply that the major exposed surfaces for pure and doped mesoporous CeO_2 remain (110) and (111) surfaces. In addition, we observed a decreased intensity of the spectra upon Y^{3+} doping (except 10%). The integrated area of the CO stretching spectra is presented in Figure 7b, which can be also interpreted as the concentration of under-coordinated Ce atoms on the surfaces. The concentration of under-coordinated Ce atoms decreased upon doping, which is due to the increased OH group bound to those sites, as indicated from XPS. The decrease of

https://doi.org/10.1021/acs.jpcc.2c04853
J. Phys. Chem. C 2022, 126, 17923−17934

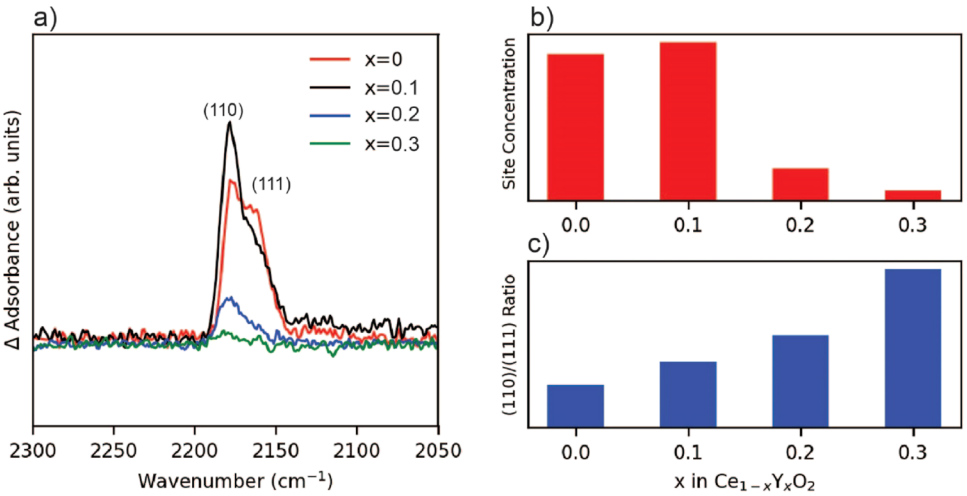

Figure 7. (a) IR characterization of CO stretching mode when CO is adsorbed on mesoporous $Ce_{1-x}Y_xO_{2-\delta}$ (x = 0, 0.1, 0.2, 0.3). (b) Undercoordinated Ce site concentration of mesoporous $Ce_{1-x}Y_xO_{2-\delta}$ (x = 0, 0.1, 0.2, 0.3). (c) (110)/(111) surface ratio of mesoporous concentration $Ce_{1-x}Y_xO_{2-\delta}$ (x = 0, 0.1, 0.2, 0.3). Graphs (b) and (c) are extracted from (a).

active sites should lead to weakened activity toward DMMP decomposition, which again agrees well with the experimental observations. The increased hydroxylation level can also explain the weaker adsorption of DMMP on mesoporous CeO_2 observed in DRIFTS measurement (red shift of ν(P═O) modes in Figure 3). Adsorption through P═O coordination onto the under-coordinated Ce atoms (P═O—Ce) is stronger than through hydrogen bonding with surface hydroxyls (i.e., P═O—HO−Ce interactions). As the level of surface hydroxylation increases, DMMP tends to adsorb more through P═O—HO−Ce interactions rather than P═O−Ce bonds, leading to weakened adsorption.

3.3.2. (110) and (111) Surfaces. The increased hydroxylation and subsequent less available active Ce/Y sites can explain the observed diminished activity of the 20 and 30% Y^{3+} samples. In the 10% doped mesoporous CeO_2, the hydroxylation level (Figure 2a) and the concentration of active undercoordinated Ce sites (Figure 7b) do not deviate significantly from that of pure mesoporous CeO_2. Indeed, the concentration of active Ce sites in the 10% doped sample slightly exceeds that of pure CeO_2. Nevertheless, we observe diminished activity in the 10% doped sample, which clearly cannot be attributed only to hydroxylation and the concentration of undercoordinated Ce sites. What leads to the decreased activity of 10% doped mesoporous CeO_2? We propose that a secondary consideration includes the type of crystallographic plane comprising the exposed surfaces of our ceria samples.

Our previous modeling of DMMP interacting with CeO_2 not only indicates that hydroxylation greatly influences the surface activity of CeO_2 but also suggests that the activity is strongly dependent on the type of facet exposed.[25] We summarize in Figure 6 surface energies, and we find that the pristine (111) surface requires significantly lower activation energy for DMMP dissociation (through P−OCH_3 cleavage) than the pristine (100) surface (24.1 vs 75.7 kJ mol^{-1}). Therefore, one expects a high ratio of (111) to (110) surfaces in CeO_2 to improve activity toward DMMP decomposition. In the 10% doped CeO_2 sample, the exposed surfaces are composed of a higher ratio of the (110) to (111) surface than in pristine CeO_2, as is shown in Figure 7a and summarized in Figure 7c. Thus, we postulate that the decrease of pristine (111) surface exposure is the major cause for the declined activity of 10% doped mesoporous CeO_2. It turns out that the (110) surface rather than the (111) surface is more exposed as the doping level grows (Figure 7c). This decrease exposure of (111) surfaces can also be part of the cause of declined activity of 20 and 30% Y^{3+}-doped mesoporous CeO_2.

Trenque et al.[23] also reported that (111) surfaces of CeO_2 nanocrystals have outstanding activity toward decomposition of DMNP, which has similar structure to DMMP. As for the reason why Y^{3+} doping leads to a change of the ratio of exposed (110) and (111) surfaces, we suspect that the doping changes the stability of the surfaces (i.e., surface energies). Theoretical work suggests that doping weakens surface polarity and thus lowers the surface energy in ZnO.[80,81] Doping might work in a similar way on CeO_2 surfaces. It seems that Y^{3+} doping changed the surface energy of (110) and (111) surfaces to different degrees. Such a change leads to a larger difference in surface energy between (110) and (111) surfaces. After doping, the (110) surface seems to have a much lower surface energy than the (111) surface. The (110) surface is corrugated and exposes either Ce or O atoms, thus leading to a polar configuration. Conversely, the (111) surface consists of both Ce and O atoms in a single plane, thus establishing a nonpolar surface.[82,83] Dopant-induced surface stabilization is more prominent in polar (110) rather than nonpolar (111) surfaces in CeO_2, leading to more exposure of the (110) surface upon Y^{3+} doping.

3.4. Consistency with La- and Gd-Doped Mesoporous CeO_2. The decreased decomposition activity of DMMP on mesoporous CeO_2 upon alio-doping not only applies on Y^{3+}-doped CeO_2 as discussed above but is also observed on La^{3+}- and Gd^{3+}-doped samples. DRIFTS measurements of DMMP on La^{3+} and Gd^{3+} show a nearly identical trend upon increasing the doping level, as is presented in Figures S16 and S17. 31P solid-state NMR La^{3+}-doped series shows similar results to Y^{3+}-doped CeO_2, as is presented in Figure S18. We cannot obtain any ^{31}P NMR signal in the Gd^{3+} series due to the strong magnetic interaction of Gd^{3+}. Since the Gd^{3+}-doped series displays a similar trend to theY^{3+} and La^{3+} series in the DRIFTS measurements, the ^{31}P solid-state NMR would not show significant deviation should the signal be observed. Both La^{3+}- and Gd^{3+}-doped mesoporous CeO_2 were also tested with

https://doi.org/10.1021/acs.jpcc.2c04853
J. Phys. Chem. C 2022, 126, 17923−17934

temperature-dependent mass spectrometry upon DMMP dosing. Consistent trends are also observed (displayed in Figure S19): methanol generated at the whole temperature range dramatically decreases upon the doping, indicating the degradation of the activity. As different dopants and various testing techniques show a consistent trend, we are convinced to say that alio-doping with 3+ valence ions (the ion has to show similar properties to Ce^{4+}) will generally deactivate the surfaces of mesoporous CeO_2 toward DMMP dissociation. Since the characterizations show that different dopants have similar effect on the surfaces of mesoporous CeO_2, we speculate that similar factors caused by alio-doping lead to the decreased activity toward DMMP decomposition.

4. CONCLUSIONS

Pure mesoporous CeO_2 possesses excellent activity to decompose DMMP at room temperature, while our study shows that a general alio-doping on CeO_2 will impede such an activity. Alio-doping can introduce oxygen vacancies in bulk CeO_2. However, the scenario becomes complicated on the surfaces. Surface oxygen vacancies introduced through alio-doping may be stabilized through hydroxylation in the ambient conditions. Preferred surface orientations can also be adjusted due to the change of the surface energy on different facets. We argued that the increased hydroxylation level as well as the change of preferred surface exposure are the major cause of degradation of the surface activity of mesoporous CeO_2 upon alio-doping. Our study provides important directions to design better CeO_2 (or possibly other metal oxides) materials for DMMP (or Sarin) decomposition: control of surface hydroxylation and preferred surface exposures. Besides alio-doping, CeO_2 can bear other categories of doping (e.g., isovalent and transition metals). Those types of doping might change the surfaces of mesoporous CeO_2 in a totally different way. Thus, though our alio-doping attempt did not improve the activity of mesoporous CeO_2 toward DMMP dissociation, other types of doping strategies might lead to the enhancement of the activity of CeO_2 and should be explored in the future.

■ ASSOCIATED CONTENT

Supporting Information

The Supporting Information is available free of charge at https://pubs.acs.org/doi/10.1021/acs.jpcc.2c04853.

TEM characterization of mesoporous doped and pure CeO_2; small-angle scattering of Gd^{3+}-doped and La^{3+} mesoporous CeO_2; nitrogen adsorption isotherm and pore size distribution of mesoporous doped and pure CeO_2; XRD of Gd^{3+}-doped and La^{3+}-doped mesoporous CeO_2; neutron diffraction and refinement of Y^{3+}-doped CeO_2; Ce 3d and O 1s XPS spectra of mesoporous doped and pure CeO_2; DRIFTS spectra of DMMP interaction with Gd^{3+}-doped and La^{3+}-doped mesoporous CeO_2; 31 P solid-state NMR of DMMP interaction with La^{3+}-doped mesoporous CeO_2; and mass spectrometry measurement of methanol production during heating cycles upon flowing DMMP through mesoporous Gd^{3+}-doped and La^{3+}-doped mesoporous CeO_2 (PDF)

■ AUTHOR INFORMATION

Corresponding Author

Efrain E. Rodriguez − *Department of Chemistry and Biochemistry, University of Maryland, College Park, Maryland 20742, United States;* orcid.org/0000-0001-6044-1543; Email: efrain@umd.edu

Authors

Tianyu Li − *Department of Chemistry and Biochemistry, University of Maryland, College Park, Maryland 20742, United States;* orcid.org/0000-0003-0142-7252

Lucas Algrim − *Department of Chemical and Environmental Engineering, University of California, Riverside, California 92521, United States*

Monica McEntee − *US Army Combat Capabilities Development Command Chemical Biological Center, Aberdeen, Maryland 21010, United States;* orcid.org/0000-0002-6127-6612

Roman Tsyshevsky − *Department of Materials Science and Engineering, University of Maryland, College Park, Maryland 20742, United States*

Matthew Leonard − *Department of Chemistry and Biochemistry, University of Maryland, College Park, Maryland 20742, United States;* orcid.org/0000-0001-7672-8418

Erin M. Durke − *US Army Combat Capabilities Development Command Chemical Biological Center, Aberdeen, Maryland 21010, United States*

Christopher Karwacki − *US Army Combat Capabilities Development Command Chemical Biological Center, Aberdeen, Maryland 21010, United States*

Maija M. Kuklja − *Department of Materials Science and Engineering, University of Maryland, College Park, Maryland 20742, United States;* orcid.org/0000-0002-5047-7734

Michael R. Zachariah − *Department of Chemical and Environmental Engineering, University of California, Riverside, California 92521, United States;* orcid.org/0000-0002-4115-3324

Complete contact information is available at: https://pubs.acs.org/10.1021/acs.jpcc.2c04853

Notes

The authors declare no competing financial interest.

■ ACKNOWLEDGMENTS

This work was funded by the Department of Defense (Grant HDTRA1-15-1-0005 and HDTRA1-19-1-0001). T.L. is grateful for the financial support from G. Forrest Woods Fellowship. We also thank the help from Dr. Fu Chen in Analytical NMR Service & Research Center at UMD for solid-state NMR measurement. The solid-state 500 MHz NMR spectrometer at UMD was supported by the NSF MRI grant (NSF-1726058). A portion of this research used resources at the Spallation Neutron Source, a DOE Office of Science User Facility operated by the Oak Ridge National Laboratory.

■ REFERENCES

(1) Li, Y. X.; Klabunde, K. J. Nano-Scale Metal Oxide Particles as Chemical Reagents. Destructive Adsorption of a Chemical Agent Simulant, Dimethyl Methylphosphonate, on Heat-Treated Magnesium Oxide. *Langmuir* **1991**, *7*, 1388−1393.

(2) Panayotov, D. A.; Morris, J. R. Uptake of a Chemical Warfare Agent Simulant (DMMP) on TiO2: Reactive Adsorption and Active Site Poisoning. *Langmuir* **2009**, *25*, 3652−3658.
(3) Yoo, R.; Yoo, S.; Lee, D.; Kim, J.; Cho, S.; Lee, W. Highly Selective Detection of Dimethyl Methylphosphonate (DMMP) Using CuO Nanoparticles /ZnO Flowers Heterojunction. *Sens. Actuators, B* **2017**, *240*, 1099−1105.
(4) Panayotov, D. A.; Morris, J. R. Thermal Decomposition of a Chemical Warfare Agent Simulant (DMMP) on TiO2: Adsorbate Reactions with Lattice Oxygen as Studied by Infrared Spectroscopy. *J. Phys. Chem. C* **2009**, *113*, 15684−15691.
(5) Gordon, W. O.; Tissue, B. M.; Morris, J. R. Adsorption and Decomposition of Dimethyl Methylphosphonate on Y2O3 Nanoparticles. *J. Phys. Chem. C* **2007**, *111*, 3233−3240.
(6) Novak, T. G.; DeSario, P. A.; Long, J. W.; Rolison, D. R. Designing Oxide Aerogels With Enhanced Sorptive and Degradative Activity for Acute Chemical Threats. *Front. Mater.* **2021**, *8*, 164.
(7) Mukhopadhyay, S.; Schoenitz, M.; Dreizin, E. L. Vapor-Phase Decomposition of Dimethyl Methylphosphonate (DMMP), a Sarin Surrogate Presence of Metal Oxides. *Def. Technol.* **2021**, *17*, 1095−1114.
(8) Head, A. R.; Tang, X.; Hicks, Z.; Wang, L.; Bleuel, H.; Holdren, S.; Trotochaud, L.; Yu, Y.; Kyhl, L.; Karslıoğlu, O.; et al. Thermal Desorption of Dimethyl Methylphosphonate from MoO3. *Catal., Struct. React.* **2017**, *3*, 112−118.
(9) Rusu, C. N.; Yates, J. T. Adsorption and Decomposition of Dimethyl Methylphosphonate on TiO2. *J. Phys. Chem. B* **2000**, *104*, 12292−12298.
(10) Segal, S. R.; Cao, L.; Suib, S. L.; Tang, X.; Satyapal, S. Thermal Decomposition of Dimethyl Methylphosphonate over Manganese Oxide Catalysts. *J. Catal.* **2001**, *198*, 66−76.
(11) Holdren, S.; Tsyshevsky, R.; Fears, K.; Owrutsky, J.; Wu, T.; Wang, X.; Eichhorn, B. W.; Kuklja, M. M.; Zachariah, M. R. Adsorption and Destruction of the G-Series Nerve Agent Simulant Dimethyl Methylphosphonate on Zinc Oxide. *ACS Catal.* **2019**, *9*, 902−911.
(12) Head, A. R.; Tsyshevsky, R.; Trotochaud, L.; Yu, Y.; Kyhl, L.; Karslloğlu, O.; Kuklja, M. M.; Bluhm, H.; Karslıoğlu, O.; Kuklja, M. M.; et al. Adsorption of Dimethyl Methylphosphonate on MoO3: The Role of Oxygen Vacancies. *J. Phys. Chem. C* **2016**, *120*, 29077−29088.
(13) Tesfai, T. M.; Sheinker, V. N.; Mitchell, M. B. Decomposition of Dimethyl Methylphosphonate (DMMP) on Alumina-Supported Iron Oxide. *J. Phys. Chem. B* **1998**, *102*, 7299−7302.
(14) Trotochaud, L.; Tsyshevsky, R.; Holdren, S.; Fears, K.; Head, A. R.; Yu, Y.; Karslloğlu, O.; Pletincx, S.; Eichhorn, B.; Owrutsky, J.; et al. Spectroscopic and Computational Investigation of Room-Temperature Decomposition of a Chemical Warfare Agent Simulant on Polycrystalline Cupric Oxide. *Chem. Mater.* **2017**, *29*, 7488−7496.
(15) Aurian-Blaieni, B.; Boucher, M. M. Interaction of Dimethyl Methylphosphonate with Metal Oxides. *Langmuir* **1989**, *5*, 170−174.
(16) Lu, G.; Zheng, H.; Lv, J.; Wang, G.; Huang, X. Review of Recent Research Work on CeO_2-Based Electrocatalysts in Liquid-Phase Electrolytes. *J. Power Sources* **2020**, *480*, No. 229091.
(17) Jaiswal, N.; Tanwar, K.; Suman, R.; Kumar, D.; Uppadhya, S.; Parkash, O. A Brief Review on Ceria Based Solid Electrolytes for Solid Oxide Fuel Cells. *J. Alloys Compd.* **2019**, *781*, 984−1005.
(18) Montini, T.; Melchionna, M.; Monai, M.; Fornasiero, P. Fundamentals and Catalytic Applications of CeO_2-Based Materials. *Chem. Rev.* **2016**, 5987−6041.
(19) Trovarelli, A. Catalytic Properties of Ceria and CeO_2-Containing Materials. *Catal. Rev.: Sci. Eng.* **1996**, *38*, 439−520.
(20) Mogensen, M.; Lindegaard, T.; Hansen, U. R.; Mogensen, G. Physical Properties of Mixed Conductor Solid Oxide Fuel Cell Anodes of Doped CeO_2. *J. Electrochem. Soc.* **1994**, *141*, 2122.
(21) Adu, K. W.; Xiong, Q.; Gutierrez, H. R.; Chen, G.; Eklund, P. C. Raman Scattering as a Probe of Phonon Confinement and Surface Optical Modes in Semiconducting Nanowires. *Appl. Phys. A: Mater. Sci. Process.* **2006**, *85*, 287−297.
(22) Trenque, I.; Magnano, G. C.; Bárta, J.; Chaput, F.; Bolzinger, M. A.; Pitault, I.; Briançon, S.; Masenelli-Varlot, K.; Bugnet, M.; Dujardin, C.; et al. Synthesis Routes of CeO_2 Nanoparticles Dedicated to Organophosphorus Degradation: A Benchmark. *CrystEngComm* **2020**, *22*, 1725−1737.
(23) Trenque, I.; Magnano, G. C.; Bolzinger, M. A.; Roiban, L.; Chaput, F.; Pitault, I.; Briançon, S.; Devers, T.; Masenelli-Varlot, K.; Bugnet, M.; Amans, D. Shape-Selective Synthesis of Nanoceria for Degradation of Paraoxon as a Chemical Warfare Simulant. *Phys. Chem. Chem. Phys.* **2019**, *21*, 5455−5465.
(24) Ederer, J.; Janoš, P.; Šťastný, M.; Henych, J.; Ederer, K.; Slušná, M. Š.; Tolasz, J. Nanocrystalline Cerium Oxide for Catalytic Degradation of Paraoxon Methyl: Influence of CeO_2 Surface Properties. *J. Environ. Chem. Eng.* **2021**, *9*, No. 106229.
(25) Li, T.; Tsyshevsky, R.; Algrim, L.; McEntee, M.; Durke, E. M.; Eichhorn, B.; Karwacki, C.; Zachariah, M. R.; Kuklja, M. M.; Rodriguez, E. E. Understanding Dimethyl Methylphosphonate Adsorption and Decomposition on Mesoporous CeO 2. *ACS Appl. Mater. Interfaces* **2021**, *13*, 54597−54609.
(26) Zhao, C.; Xu, Y. Theoretical Investigation of Dephosphorylation of Phosphate Monoesters on CeO_2(111). *Catal. Today* **2018**, *312*, 141−148.
(27) Salerno, A.; Pitault, I.; Devers, T.; Pelletier, J.; Briançon, S. Model-Based Optimization of Parameters for Degradation Reaction of an Organophosphorus Pesticide, Paraoxon, Using CeO_2 Nanoparticles in Water Media. *Environ. Toxicol. Pharmacol.* **2017**, *53*, 18−28.
(28) Chen, D. A.; Ratliff, J. S.; Hu, X.; Gordon, W. O.; Senanayake, S. D.; Mullins, D. R. Dimethyl Methylphosphonate Decomposition on Fully Oxidized and Partially Reduced Ceria Thin Films. *Surf. Sci.* **2010**, *604*, 574−587.
(29) Arabac, A.; Öksüzömer, M. F. Preparation and Characterization of 10 Mol% Gd Doped CeO_2 (GDC) Electrolyte for SOFC Applications. *Ceram. Int.* **2012**, *38*, 6509−6515.
(30) Liyanage, A. D.; Perera, S. D.; Tan, K.; Chabal, Y.; Balkus, K. J. Synthesis, Characterization, and Photocatalytic Activity of Y-Doped CeO_2 Nanorods. *ACS Catal.* **2014**, *4*, 577−584.
(31) Truffault, L.; Ta, M. T.; Devers, T.; Konstantinov, K.; Harel, V.; Simmonard, C.; Andreazza, C.; Nevirkovets, I. P.; Pineau, A.; Veron, O.; et al. Application of Nanostructured Ca Doped CeO_2 for Ultraviolet Filtration. *Mater. Res. Bull.* **2010**, *45*, 527−535.
(32) Wen, Q. Y.; Zhang, H. W.; Song, Y. Q.; Yang, Q. H.; Zhu, H.; Xiao, J. Q. Room-Temperature Ferromagnetism in Pure and Co Doped Powders. *J. Phys.: Condens. Matter* **2007**, *19*, No. 246205.
(33) Deng, C.; Huang, Q.; Zhu, X.; Hu, Q.; Su, W.; Qian, J.; Dong, L.; Li, B.; Fan, M.; Liang, C. The Influence of Mn-Doped CeO_2 on the Activity of CuO/CeO_2 in CO Oxidation and NO + CO Model Reaction. *Appl. Surf. Sci.* **2016**, *389*, 1033−1049.
(34) Ruiz-Trejo, E. The Optical Band Gap of Gd-Doped CeO_2 Thin Films as Function of Temperature and Composition. *J. Phys. Chem. Solids* **2013**, *74*, 605−610.
(35) Yue, L.; Zhang, X. M. Structural Characterization and Photocatalytic Behaviors of Doped CeO_2 Nanoparticles. *J. Alloys Compd.* **2009**, *475*, 702−705.
(36) Goto, Y.; Takahashi, K.; Omata, T.; Otsuka-Yao-Matsuo, S. Synthesis of Y2O3-Doped CeO_2 Nanocrystals and Their Surface Modification. *J. Phys.: Conf. Ser.* **2009**, *165*, 12041.
(37) Inaba, H.; Tagawa, H. Ceria-Based Solid Electrolytes. *Solid State Ionics* **1996**, *83*, 1−16.
(38) Mori, T.; Drennan, J.; Lee, J. H.; Li, J. G.; Ikegami, T. Oxide Ionic Conductivity and Microstructures of Sm- or La-Doped CeO_2-Based Systems. *Solid State Ionics* **2002**, *154*−*155*, 461−466.
(39) Otero, G. S.; Lustemberg, P. G.; Prado, F.; Ganduglia-Pirovano, M. V. Relative Stability of Near-Surface Oxygen Vacancies at the CeO_2(111) Surface upon Zirconium Doping. *J. Phys. Chem. C* **2020**, *124*, 625.
(40) Zhang, W.; Pu, M.; Lei, M. Theoretical Studies on the Stability and Reactivity of the Metal-Doped CeO_2(100) Surface: Toward H2

Dissociation and Oxygen Vacancy Formation. *Langmuir* **2020**, *36*, 5891−5901.
(41) Murakami, K.; Ogo, S.; Ishikawa, A.; Takeno, Y.; Higo, T.; Tsuneki, H.; Nakai, H.; Sekine, Y. Heteroatom Doping Effects on Interaction of H2O and CeO_2 (111) Surfaces Studied Using Density Functional Theory: Key Roles of Ionic Radius and Dispersion. *J. Chem. Phys.* **2020**, *152*, 14707.
(42) Kossoy, A.; Cohen, H.; Bendikov, T.; Wachtel, E.; Lubomirsky, I. Water Adsorption at the Surface of Pure and Gd-Doped Ceria. *Solid State Ionics* **2011**, *194*, 1−4.
(43) Fronzi, M.; Piccinin, S.; Delley, B.; Traversa, E.; Stampfl, C. Water Adsorption on the Stoichiometric and Reduced CeO_2(111) Surface: A First-Principles Investigation. *Phys. Chem. Chem. Phys.* **2009**, *11*, 9188−9199.
(44) Pintos, D. G.; Juan, A.; Irigoyen, B. Density Functional Theory Study of Water Interactions on Mn-Doped CeO 2 (1 1 1) Surface. *Appl. Surf. Sci.* **2014**, *313*, 784−793.
(45) Le Gal, A.; Abanades, S. Dopant Incorporation in Ceria for Enhanced Water-Splitting Activity during Solar Thermochemical Hydrogen Generation. *J. Phys. Chem. C* **2012**, *116*, 13516−13523.
(46) Chen, B.; Ma, Y.; Ding, L.; Xu, L.; Wu, Z.; Yuan, Q.; Huang, W. Reactivity of Hydroxyls and Water on a CeO_2(111) Thin Film Surface: The Role of Oxygen Vacancy. *J. Phys. Chem. C* **2013**, *117*, 5800−5810.
(47) Li, M.; Tumuluri, U.; Wu, Z.; Dai, S. Effect of Dopants on the Adsorption of Carbon Dioxide on Ceria Surfaces. *ChemSusChem* **2015**, *8*, 3651−3660.
(48) Spezzati, G.; Benavidez, A. D.; DeLaRiva, A. T.; Su, Y.; Hofmann, J. P.; Asahina, S.; Olivier, E. J.; Neethling, J. H.; Miller, J. T.; Datye, A. K.; et al. CO Oxidation by Pd Supported on CeO_2(100) and CeO_2(111) Facets. *Appl. Catal., B* **2019**, *243*, 36−46.
(49) Baumann, N.; Lan, J.; Iannuzzi, M. CO2adsorption on the Pristine and Reduced CeO_2(111) Surface: Geometries and Vibrational Spectra by First Principles Simulations. *J. Chem. Phys.* **2021**, *154*, 94702.
(50) Zhang, W.; Pu, M.; Lei, M. Theoretical Studies on the Stability and Reactivity of the Metal-Doped CeO_2(100) Surface: Toward H2Dissociation and Oxygen Vacancy Formation. *Langmuir* **2020**, *36*, 5891−5901.
(51) Laha, S. C.; Ryoo, R. Synthesis of Thermally Stable Mesoporous Cerium Oxide with Nanocrystalline Frameworks Using Mesoporous Silica Templates. *Chem. Commun.* **2003**, *3*, 2138−2139.
(52) Ji, P.; Zhang, J.; Chen, F.; Anpoa, M. Ordered Mesoporous CeO_2 Synthesized by Nanocasting from Cubic Ia3d Mesoporous MCM-48 Silica: Formation, Characterization and Photocatalytic Activity. *J. Phys. Chem. C* **2008**, *112*, 17809−17813.
(53) Kim, T.-W.; Kleitz, F.; Paul, B.; Ryoo, R. MCM-48-like Large Mesoporous Silicas with Tailored Pore Structure: Facile Synthesis Domain in a Ternary Triblock Copolymer−Butanol−Water System. *J. Am. Chem. Soc.* **2005**, *127*, 7601−7610.
(54) Cheary, R. W.; Coelho, A. Fundamental Parameters Approach to X-Ray Line-Profile Fitting. *J. Appl. Crystallogr.* **1992**, *25*, 109−121.
(55) Harvey, J. A.; McEntee, M. L.; Garibay, S. J.; Durke, E. M.; DeCoste, J. B.; Greathouse, J. A.; Sava Gallis, D. F. Spectroscopically Resolved Binding Sites for the Adsorption of Sarin Gas in a Metal-Organic Framework: Insights beyond Lewis Acidity. *J. Phys. Chem. Lett.* **2019**, *10*, 5142−5147.
(56) Gibbons, W. T.; Holdren, S.; Hu, J.; Eichhorn, B. W.; Zachariah, M. R. Fixed Feed Temperature-Programmed Modulation − A Quantitative Method to Obtain Thermophysical Parameters: Application to Chemical Warfare Agent Adsorbents. *J. Phys. Chem. C* **2019**, *123*, 12694−12705.
(57) McBride, J. R.; Hass, K. C.; Poindexter, B. D.; Weber, W. H. Raman and X-Ray Studies of Ce1-XRExO2-y, Where RE = La, Pr, Nd, Eu, Gd, and Tb. *J. Appl. Phys.* **1994**, *76*, 2435−2441.
(58) Coduri, M.; Scavini, M.; Allieta, M.; Brunelli, M.; Ferrero, C. Local Disorder in Yttrium Doped Ceria (Ce1-XYxO 2-x/2) Probed by Joint X-Ray and Neutron Powder Diffraction. *J. Phys.: Conf. Ser.* **2012**, *340*, No. 012056.
(59) Guo, M.; Lu, J.; Wu, Y.; Wang, Y.; Luo, M. UV and Visible Raman Studies of Oxygen Vacancies in Rare-Earth-Doped Ceria. *Langmuir* **2011**, *27*, 3872−3877.
(60) Paparazzo, E. Use and Mis-Use of x-Ray Photoemission Spectroscopy Ce3d Spectra of Ce_2O_3 and CeO_2. *J. Phys.: Condens. Matter* **2018**, *30*, 343003.
(61) Stroppa, D. G.; Dalmaschio, C. J.; Houben, L.; Barthel, J.; Montoro, L. A.; Leite, E. R.; Ramirez, A. J. Analysis of Dopant Atom Distribution and Quantification of Oxygen Vacancies on Individual Gd-Doped CeO_2 Nanocrystals. *Chem. −Eur. J.* **2014**, *20*, 6288−6293.
(62) Huber, A. K.; Falk, M.; Rohnke, M.; Luerssen, B.; Amati, M.; Gregoratti, L.; Hesse, D.; Janek, J. In Situ Study of Activation and De-Activation of LSM Fuel Cell Cathodes - Electrochemistry and Surface Analysis of Thin-Film Electrodes. *J. Catal.* **2012**, *294*, 79−88.
(63) Fister, T. T.; Fong, D. D.; Eastman, J. A.; Baldo, P. M.; Highland, M. J.; Fuoss, P. H.; Balasubramaniam, K. R.; Meador, J. C.; Salvador, P. A. In Situ Characterization of Strontium Surface Segregation in Epitaxial La0.7Sr0.3MnO3 Thin Films as a Function of Oxygen Partial Pressure. *Appl. Phys. Lett.* **2008**, *93*, 151904.
(64) Li, Y.; Zhang, W.; Zheng, Y.; Chen, J.; Yu, B.; Chen, Y.; Liu, M. Controlling Cation Segregation in Perovskite-Based Electrodes for High Electro-Catalytic Activity and Durability. *Chem. Soc. Rev.* **2017**, 6345−6378.
(65) Hess, F.; Yildiz, B. Polar or Not Polar? The Interplay between Reconstruction, Sr Enrichment, and Reduction at the La0.75Sr0.25MnO3 (001) Surface. *Phys. Rev. Mater.* **2020**, *4*, No. 015801.
(66) Koo, B.; Kim, K.; Kim, J. K.; Kwon, H.; Han, J. W.; Jung, W. C. Sr Segregation in Perovskite Oxides: Why It Happens and How It Exists. *Joule* **2018**, *2*, 1476−1499.
(67) Crumlin, E. J.; Mutoro, E.; Liu, Z.; Grass, M. E.; Biegalski, M. D.; Lee, Y. L.; Morgan, D.; Christen, H. M.; Bluhm, H.; Shao-Horn, Y. Surface Strontium Enrichment on Highly Active Perovskites for Oxygen Electrocatalysis in Solid Oxide Fuel Cells. *Energy Environ. Sci.* **2012**, *5*, 6081−6088.
(68) Moss, J. A.; Szczepankiewicz, S. H.; Park, E.; Hoffmann, M. R. Adsorption and Photodegradation of Dimethyl Methylphosphonate Vapor at TiO 2 Surfaces. *J. Phys. Chem. B* **2005**, *109*, 19779−19785.
(69) Templeton, M. K.; Weinberg, W. H. Adsorption and Decomposition of Dimethyl Methylphosphonate on an Aluminum Oxide Surface. *J. Am. Chem. Soc.* **1985**, *107*, 97−108.
(70) Jeon, S.; Schweigert, I. V.; Pehrsson, P. E.; Balow, R. B. Kinetics of Dimethyl Methylphosphonate Adsorption and Decomposition on Zirconium Hydroxide Using Variable Temperature in Situ Attenuated Total Reflection Infrared Spectroscopy. *ACS Appl. Mater. Interfaces* **2020**, *12*, 14662−14671.
(71) Joseph, J.; Jemmis, E. D. Red-, Blue-, or No-Shift in Hydrogen Bonds: A Unified Explanation. *J. Am. Chem. Soc.* **2007**, *129*, 4620−4632.
(72) Wright, A. M.; Howard, A. A.; Howard, J. C.; Tschumper, G. S.; Hammer, N. I. Charge Transfer and Blue Shifting of Vibrational Frequencies in a Hydrogen Bond Acceptor. *J. Phys. Chem. A* **2013**, *117*, 5435−5446.
(73) Sambur, J. B.; Doetschman, D. C.; Yang, S. W.; Schulte, J. T.; Jones, B. R.; DeCoste, J. B. Multiple Effects of the Presence of Water on the Nucleophilic Substitution Reactions of NaX Faujasite Zeolite with Dimethyl Methylphosphonate (DMMP). *Microporous Mesoporous Mater.* **2008**, *112*, 116−124.
(74) Yang, S. W.; Doetschman, D. C.; Schulte, J. T.; Sambur, J. B.; Kanyi, C. W.; Fox, J. D.; Kowenje, C. O.; Jones, B. R.; Sherma, N. D. Sodium X-Type Faujasite Zeolite Decomposition of Dimethyl Methylphosphonate (DMMP) to Methylphosphonate: Nucleophilic Zeolite Reactions I. *Microporous Mesoporous Mater.* **2006**, *92*, 56−60.
(75) Hung, W. C.; Wang, J. C.; Wu, K. H. Adsorption and Decomposition of Dimethyl Methylphosphonate (DMMP) on Expanded Graphite/Metal Oxides. *Appl. Surf. Sci.* **2018**, *444*, 330−335.
(76) Knagge, K.; Johnson, M.; Grassian, V. H.; Larsen, S. C. Adsorption and Thermal Reaction of DMMP in Nanocrystalline NaY. *Langmuir* **2006**, *22*, 11077−11084.

https://doi.org/10.1021/acs.jpcc.2c04853
J. Phys. Chem. C 2022, 126, 17923−17934

(77) Mitchell, M. B.; Sheinker, V. N.; Tesfamichael, A. B.; Gatimu, E. N.; Nunley, M. Decomposition of Dimethyl Methylphosphonate (DMMP) on Supported Cerium and Iron Co-Impregnated Oxides at Room Temperature. *J. Phys. Chem. B* **2003**, *107*, 580−586.
(78) Wang, Y.; Wöll, C. IR Spectroscopic Investigations of Chemical and Photochemical Reactions on Metal Oxides: Bridging the Materials Gap. *Chem. Soc. Rev.* **2017**, *46*, 1875−1932.
(79) Yang, C.; Yu, X.; Heißler, S.; Nefedov, A.; Colussi, S.; Llorca, J.; Trovarelli, A.; Wang, Y.; Wöll, C. Surface Faceting and Reconstruction of Ceria Nanoparticles. *Angew. Chem., Int. Ed.* **2017**, *56*, 375−379.
(80) Lahmer, M. A. The Effect of Doping with Rare Earth Elements (Sc, Y, and La) on the Stability, Structural, Electronic and Photocatalytic Properties of the O-Termintaed ZnO Surface; a First-Principles Study. *Appl. Surf. Sci.* **2018**, *457*, 315−322.
(81) Erker, S.; Rinke, P.; Moll, N.; Hofmann, O. T. Doping Dependence of the Surface Phase Stability of Polar O-Terminated $(000\bar{1})$ ZnO. *New J. Phys.* **2017**, *19*, No. 083012.
(82) Wardenga, H. F.; Klein, A. Surface Potentials of (111), (110) and (100) Oriented CeO_{2-x} Thin Films. *Appl. Surf. Sci.* **2016**, *377*, 1−8.
(83) Désaunay, T.; Ringuedé, A.; Cassir, M.; Labat, F.; Adamo, C. Modeling Basic Components of Solid Oxide Fuel Cells Using Density Functional Theory: Bulk and Surface Properties of CeO_2. *Surf. Sci.* **2012**, *606*, 305−311.

https://doi.org/10.1021/acs.jpcc.2c04853
J. Phys. Chem. C 2022, 126, 17923−17934